International Journal of Engineering & Scientific Research
Vol. 10 Issue 10, October 2022,
ISSN: 2347-6532 Impact Factor: 6.660
Journal Homepage: http://esrjournal.com, Email: esrjeditor@gmail.com
Double-Blind Peer Reviewed Refereed Open Access International Journal - Included in the International Serial Directories Indexed & Listed at: Ulrich's Periodicals Directory ©, U.S.A., Open J-Gage as well as in Cabell's Directories of Publishing Opportunities, U.S.A

NANOSTRUCTURING TIN OXIDE WITH ORGANIC LIGANDS FOR OPTOELECTRONICS

Dr. Deepanshi Khatri
Address: H.No. 1373, Sector 14, Hisar (Haryana)
Mail ID: deepanshi07@rediffmail.com

ABSTARCT

Tin oxide (SnO_2) nanoparticles with remarkable characteristics can now be synthesized using a fresh and revolutionary technique. SnO_2's desirable properties as a catalyst, battery, and window coating include its high conductivity, stability, and transparency. This non-aqueous sol-gel synthesis method produces a narrow particle size distribution without the need of surfactants or heat treatments. This single-pot procedure is also temperature-tolerant, making it suitable for usage with plastic films.

Powder X-ray diffraction and high-resolution transmission electron microscopy were used to examine the SnO_2 nanoparticles and determine their size distribution, shape, and dislocation density, among other properties. As can be seen from the results, the average particle size of the NPs was somewhere in the range of 3.4 to 7.7 nm. Nuclear magnetic resonance, Fourier transform infrared, and Raman spectroscopy further investigated the materials and confirmed the presence of organic molecules produced from the 1-hexanol reactant. Using UV-visible spectroscopy, researchers looked at the absorbing properties of SnO_2 NPs and discovered that the band gap went down in energy with decreasing particle size. Mechanical forces within the tiniest NPs, perhaps related to the organic ligands covering their surface, may account for this unexpected finding. A higher density of screw dislocations was shown to correlate with larger NP sizes, suggesting stress relief. This novel strategy has the potential to offer an alternative to using chemical dopants in order to tune the band gap of SnO_2 NPs.

Keywords*:* *Powder X-ray diffraction, Dopants, Nuclear Magnetic resonance, Fourier Transform Infrared, and Raman Spectroscopy*

INTRODUCTION

The synthesis of nanoparticles has been an area of intense research in recent years, owing to their unique physical and chemical properties, which are different from those of bulk materials. Tin dioxide (SnO_2) nanoparticles have received particular attention due to their wide range of applications in fields such as gas sensing, solar cells, and catalysis. In recent years, the sol-gel method has emerged as a promising technique for the synthesis of nanoparticles, owing to its simplicity, cost-effectiveness, and ability to produce nanoparticles with controlled size and morphology.

This paper presents a study on the one-step synthesis, structure, and band gap properties of SnO_2 nanoparticles made by a low temperature nonaqueous sol-gel technique. The authors describe the synthesis process, which involves the use of a nonaqueous solvent and a low-temperature annealing step. They then present the characterization of the nanoparticles using techniques such as X-ray diffraction (XRD), transmission electron microscopy (TEM), and UV-Vis spectroscopy. The results of the study reveal that the SnO_2 nanoparticles synthesized by this method have a uniform size distribution and a crystalline structure, with an average particle size in the range of 5-10 nm. The authors also investigate the band gap properties of the nanoparticles, which is an important factor that affects their optical and electronic properties. They measure the band gap using UV-Vis spectroscopy and find that it is in the range of 3.6-3.8 eV, which is consistent with the band gap of SnO_2 nanoparticles reported in previous studies. The authors discuss the

implications of these results and their potential applications in areas such as gas sensing, solar cells, and catalysis.

REVIEW OF RELATED LITERATURE

Srinivasan and Kannan (2016) synthesized and characterized SnO2 nanoparticles using a nonaqueous sol-gel method. The authors investigated the effect of annealing temperature on the size and crystallinity of the nanoparticles. They found that the SnO_2 nanoparticles synthesized at 500°C had a smaller particle size and a more crystalline structure.

Ravichandran and Prakash (2018) reported the synthesis of SnO_2 nanoparticles using a low-temperature nonaqueous sol-gel technique. The authors investigated the effect of precursor concentration and annealing temperature on the size and morphology of the nanoparticles. They found that the SnO_2 nanoparticles synthesized at 400°C had a uniform size distribution and a spherical morphology.

Sivakumar and Ramasamy (2019) synthesized SnO_2 nanoparticles using a nonaqueous sol-gel method and investigated their structural, optical, and electrical properties. The authors found that the SnO_2nanoparticles had a crystalline structure and a band gap of 3.6 eV. They also found that the electrical conductivity of the nanoparticles increased with increasing annealing temperature.

Rathod and Jadhav (2020) reported the synthesis of SnO_2 nanoparticles using a nonaqueous sol-gel technique and investigated their structural and optical properties. The authors found that the SnO_2 nanoparticles had a crystalline structure and a band gap of 3.7 eV. They also found that the nanoparticles had good photocatalytic activity for the degradation of methylene blue dye.

Chakraborty, Chakrabarty, and Dutta (2021) reported the synthesis of SnO_2nanoparticles using a nonaqueous sol-gel technique and investigated their photocatalytic activity. The authors found that the SnO_2 nanoparticles had a uniform size distribution and a crystalline structure. They also found that the nanoparticles had good photocatalytic activity for the degradation of rhodamine B dye.

EXPERIMENTAL INVESTIGATION

SnO_2 NPs synthesis. We used Aldrich-obtained tin(IV) chloride (99.995%) and anhydrous 1-hexanol (99%). The synthesis was done in a glovebox with extremely low oxygen and humidity levels (1 ppm). The standard operating procedure calls for 1 mmol (0.2603 g) of tin(IV) chloride to be added to 20 mL of 1-hexanol before being sealed in an autoclave made of stainless steel. After three days of heating in a furnace at 160–260 °C, the autoclave was removed from the glovebox. Centrifuging the resultant milky suspensions, washing the precipitates with ethanol and dichloromethane, and drying them in air at 60 °C yielded usable powder.Definition of the Sample. X-ray powder diffraction (XRPD) measurements of SnO_2 NPs were carried out using a / diffractometer (PANanalytical X'Pert Pro, NL) fitted with a fast RTMS detector and Cu K radiation (45 kV, 40 mA) in the 20-125° 2 θ range, with a virtual step scan of 0.1° 2 θ and a virtual duration per step of 500 s. Using the PM2K software package, the diffraction profiles were analyzed using the WPPM method,. By adjusting model parameters using a nonlinear least squares fitting approach, based on the profile of the experimental data, this cutting-edge novel method may retrieve microstructural information from a powder diffraction pattern.

Background (modelled with a 4th-order shifted Chebyshev polynomial function), peak intensities, specimen displacement, mean and variance of the NP size distributions, and lattice parameters were all refined through WPPM modelling of the data after the addition of SnO_2 described within space group $P4_Z/mnm$ for the tetragonal rutile structure. The diameter of the crystalline diffracting domains was assumed to follow a log-normal distribution for the sake of simplicity. As shown by Koffyberg [Burgers vector equal to $(a_0^2 + c^2)^{1/2}$, with a_0 and c_0 being the lattice parameters] and recently validated by

Scardi's group using the WPPM method, it was originally assumed that the slip system contained both edge and screw dislocations with densities of e and s, respectively. Based on our HRTEM images (see below), we hypothesised that the only source of anisotropy in the XRPD line profile broadening was the presence of screw dislocations in the NPs. Point-to-point and line-to-line resolutions of 0.28 and 0.14 nm were achieved during transmission electron microscopy (TEM) with a Jeol-2000 FXII microscope. The JEOL 2200FS microscope, equipped with a field-emission gun, was used to capture additional HRTEM pictures at 200 kV. Drops of a suspension containing the NPs were evaporated on carbon-coated Cu grids before being used as samples for transmission electron microscopy (TEM) and high-resolution transmission electron microscopy (HRTEM) observations.

$$\alpha \approx \frac{k}{S} = \frac{(1 - R_\infty)^2}{2R_\infty} \equiv F(R_\infty)$$

To learn more about the organic species that generated during the reaction and were retained in the supernatant liquid after centrifugation, ^{1}H and ^{13}C NMR spectroscopies were performed on the liquid. The 300 MHz Bruker AVANCE NMR spectrometer was used to take spectra of $CDCl_3$ solutions. The SnO_2 NPs were investigated using solid-state NMR investigations on a Bruker AVANCE 300 spectrometer equipped with a 7.05 T wide-bore magnet at ambient probe temperature. Using a typical Bruker 4 mm double-resonance MAS probe, high-resolution solid-state ^{1}H, ^{13}C, and 119Sn NMR spectra were obtained at 300.1, 75.5, and 111.9 MHz, respectively. With a stability of better than 3 Hz, zirconia rotors with an exterior diameter of 4 mm were used to spin powdered solid materials at MAS frequencies of 3–12 kHz. Using MAS, high-power proton decoupling, and the pulse sequence of Cory and Ritchey to suppress signals from materials outside the NMR coil, high-resolution solid-state ^{13}C NMR spectra were acquired. The following describes the usual setup for ^{13}C NMR investigations during the acquisition phase: Recycle delay = 10 s; number of transients = 6000-17 200; pulse duration = 3.0 s at 90 degrees for ^{13}C. The following collection parameters were used to collect solid-state ^{13}C MAS spectra with high-power proton decoupling and cross-polarization (CP) from protons for the sample produced at 200 °C: Recycle delay = 5 s; number of transients = 3400; duration of ^{1}H 90° pulse = 4.0 s. Despite the direct identification of ^{13}C nuclei, the signal-to-noise ratio of the ^{13}C CPMAS spectrum was lower than that obtained using the sequence of Cory and Ritchey. The following acquisition circumstances were used to capture solid-state 119Sn MAS spectra at 111.9 MHz with and without high-power proton decoupling: The duration of a 60-degree 119Sn pulse is 1.5 s, the recycle delay is 1030 s, the number of transients is 2,000–30,000, and the MAS frequency is 3.1–12.kHz. The following acquisition circumstances were used to record 119Sn SSNMR spectra on a Bruker AVANCE 600 MHz spectrometer at the resonance frequency of 223.8 MHz: There were 1,500 to 12,300 transients and a MAS frequency of 10 to 12 kilohertz for a 45 degree pulse of 119Sn. A single pulse stimulation lasting 2.4 s (recycle delay = 5 s; number of transients = 832; and MAS frequency = 812 kHz) was utilised to acquire 1H MAS NMR spectra at 300.1 MHz. The ^{13}C chemical shift (176.46 ppm) and 1H chemical shift (0 ppm) were calibrated against tetramethylsilane (TMS) using glycine and tetrakis(trimethylstannyl)methane, respectively. Tetrakis- (trimethylstannyl)methane $C(SnMe_3)_4$ (48.2 ppm) is used as a standard to provide the 119Sn chemical shifts in relation to tetramethyltin SnMe4. In the case of the ^{119}Sn CSA ($\Delta\delta$) for SnO2 with $\delta < 0$, parameters are defined as follows

Principal CSA components $\delta_{11} \geq \delta_{22} \geq \delta_{33}$

Isotropic value $\delta_{iso} = (\delta_{11} + \delta_{22} + \delta_{33})/3$

Chemical shift anisotropy $\Delta\delta = \delta_{33} - (\delta_{11} + \delta_{22})/2$

Asymmetry parameter $\eta = (\delta_{22} - \delta_{11})/(\delta_{33} - \delta_{iso})$ with $0 \leq \eta \leq 1$

RESULTS AND DISCUSSION

Both HRTEM and X-ray diffraction were used. X-ray analysis (Figure 1) confirmed that the SnO_2 NPs crystallised in the rutile structure (space group $P4_Z/mnm$) without the presence of any other impurity phases. First glances at the XRPD patterns show that as NP size and synthesis temperature were increased, the peaks got more distinct and sharp. The resulting XRPD profiles were analysed using WPPM. In addition to solving size and defect concentration in SnO_2, this method has been used recently to obtain data on the average crystalline domain size of the NPs (Table 1 and Fig. 2).

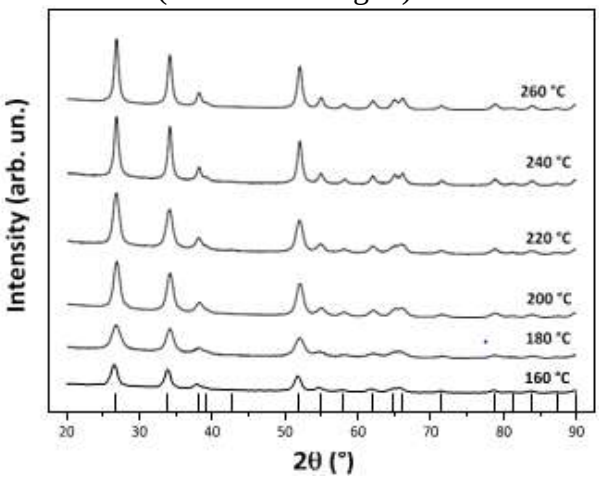

Fig. 1. Powder X-ray diffraction patterns (Cu Kα radiation) of the SnO_2 specimens prepared at different temperatures. The vertical lines below indicate the expected reflections for the rutile structured cassiterite phase.

Table 1. Results of WPPM Modeling and Refinement from the X-ray Powder Diffraction Data, Including Unit Cell Parameters, Tetragonality (c/a), Crystalline Domain Diameters (Average, Mode, and Skewness of the log-Normal Size Distribution), and Dislocation Densities (Edge and Screw, ρ_e and ρ_s, Respectively) of Synthesized SnO_2 NPs

		agreement factors			unit cell parameters (nm)			crystalline domain diameter			dislocation density ($\times 10^{15}$ m^{-2})	
synthesis temperature (˚C)		R_{wp} (%)	R_{exp} (%)	χ^2	c (nm)	volume (nm^3)	c/a	average	mode	skewness	ρ_e	ρ_s
160	2.25	1.38	1.64	0.4751(1)	0.3185(1)	0.072(1)	0.6703	3.4(1)	2.3(1)	1.7(1)	1.0(7)	1.3(1)
180	1.85	1.34	1.38	0.4749(1)	0.3186(1)	0.072(1)	0.6709	5.3(2)	3.1(1)	2.2(1)	1.0(5)	1.2(8)
200	2.20	1.68	1.31	0.4750(1)	0.3189(1)	0.072(1)	0.6713	6.2(4)	4.9(3)	1.3(1)	1.0(7)	1.4(1)
220	1.94	1.33	1.46	0.4748(1)	0.3190(1)	0.072(1)	0.6719	6.9(2)	5.7(2)	1.1(1)	1.0(1)	1.7(2)
240	2.03	1.34	1.51	0.4748(1)	0.3188(1)	0.072(1)	0.6714	7.2(3)	5.0(2)	1.7(1)	1.0(3)	1.9(5)
260	2.04	1.31	1.56	0.4749(1)	0.3189(1)	0.072(2)	0.6714	7.7(1)	6.7(1)	0.9(1)	1.0(5)	1.9(2)

Figure 2 shows that the residual line is nearly flat, indicating good agreement between the experiment and the model and supporting the idea that the SnO_2 nanodomains under study have a spherical form. Particle size distributions derived from the HRTEM pictures reported below correspond in general with the log-normal size

distributions of the SnO_2 NPs synthesised at different temperatures as shown in Figure 3.

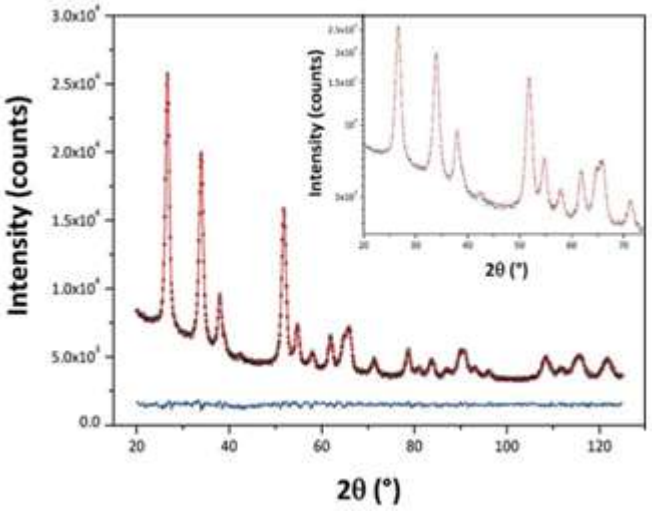

Fig. 2. Typical output of the WPPM modeling protocol applied to the observed X-ray diffraction pattern of a specimen synthesized at 220^0C

While TEM image analysis is useful, we find that the data and modelling from X-ray diffraction provide a more statistically representative selection of the entire specimens. Small variations in the tetragonal distortion of the SnO_2 unit cell were detected, principally an increase in the c/a ratio with increasing synthesis temperature (Table 1), but the unit cell volumes did not change considerably as a function of synthesis temperature. The WPPM investigation of SnO_2 at 160 °C revealed an average crystalline domain width of 3.4 nm, with a tail in the log-normal size distribution function extending to 10 nm (Table 1, Figure 3). The average crystalline domain diameter increased from 6.9 nm at 220 °C to 7.7 nm at 260 °C as the synthesis temperature was raised. Table 1 and Figure 3 both reveal that the probability distributions are positively skewed, with some spread towards bigger NP sizes at the tails. In every sample tested (Table 1), the number of screw dislocations "e" was found to be higher than the number of edge dislocations. As the synthesis temperature was raised, the density of screw dislocations "s" increased somewhat, whereas the number of edge dislocations remained constant. For 180 °C synthesis, the screw dislocation population showed a larger dispersion around the mean (Fig. 4).

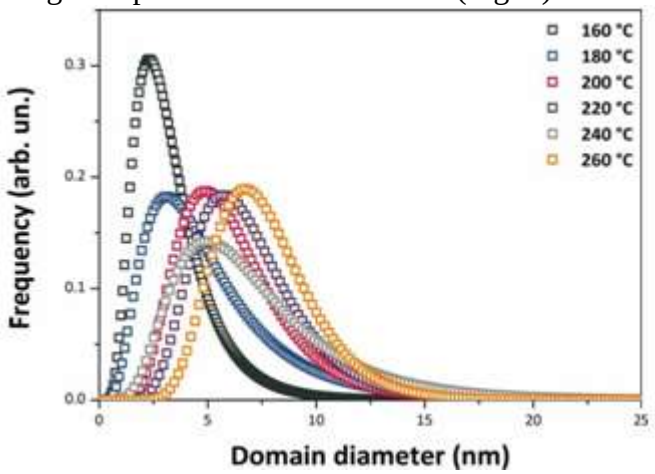

Fig. 3: SnO_2 NP size distributions obtained from WPPM modeling

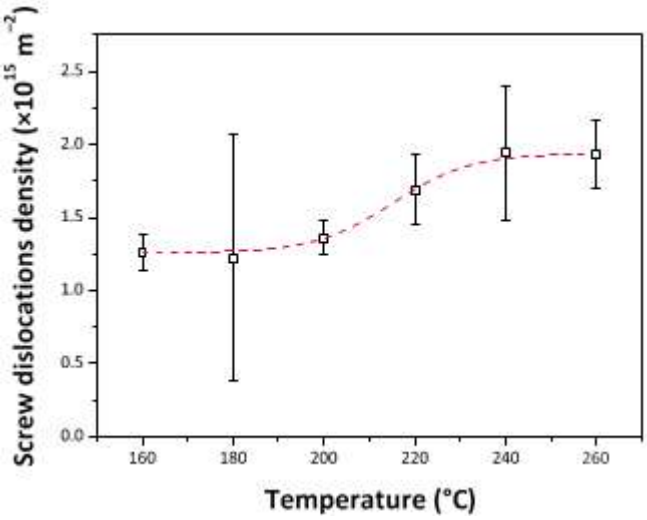

Fig. 4: Evolution of screw dislocation densities with the synthesis temperature. The red dashed line represents a sigmoidal fit obtain using a sigmoidal Boltzmann function (R_2 = 0.997).

Using HRTEM, we further explored (Figure 5 and Table 2) how the synthesis temperature affected the resulting SnO_2 NPs' size, shape, and defect development. Our WPPM analysis of the XRPD data confirms that all of the NPs displayed a high degree of crystallinity, with lattice fringes matching the cell parameters of rutile-estimated from the recorded images ranging between 2 and 11 nm. This is in line with the overall average provided by that analysis, which is based on a more comprehensive sample size.

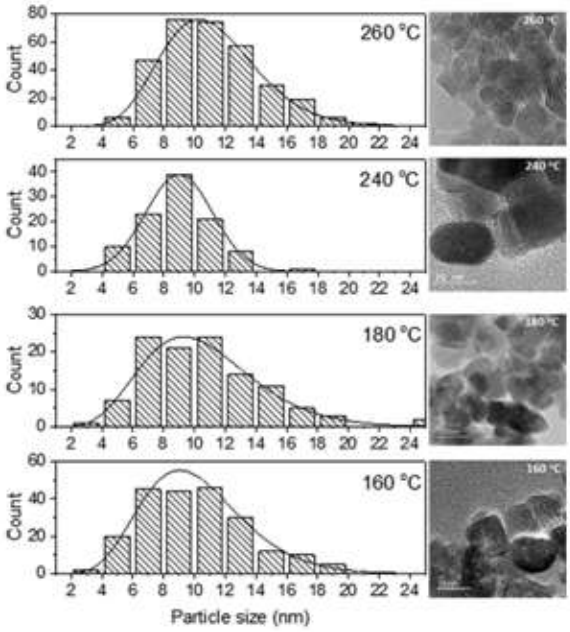

Fig. 5: Particle size distribution (left) of SnO_2 NPs prepared at 160, 180, 240, and 260 °C from the analysis of HRTEM images (right).

Table 2. HRTEM Particle Size Distributions Obtained by Analysis of Images for Samples Prepared at 160, 180, 240, and 260 °C

temperature (°C)	average size (nm)	minimum size (nm)	maximum size (nm)	standard deviation
160	10.2	4.0	19.5	3.4
180	10.6	4.0	24.7	3.9
240	9.0	4.50	17.3	2.2
260	11.2	4.7	21.2	3.1

Nuclear magnetic resonance spectroscopy in the liquid phase. Liquid ^{1}H and ^{13}C NMR spectroscopy was used to investigate the 1-hexanol-$SnCl_4$ synthesis reaction after the supernatant liquid was filtered to eliminate the solid SnO_2 precipitate. Figure 7 displays the ^{13}C NMR spectrum (1H NMR spectra can be found in Figure S1 in the supplementary materials). The presence of 1-hexanol (62.8 ppm for the C1 carbon), dihexyl ether (71.1 ppm), and 1-chlorohexane (45.1 ppm for the C1 carbon) was deduced from this spectrum's analysis (Table S1). In the same area, between 14 and 33 ppm, are all of the other peaks from these three hydrocarbons, which correspond to carbons C2 through C6 in hexane. Analysis of the solid-state ^{13}C MAS NMR spectra, as described below, allowed us to infer the production of the dihexyl ether component.

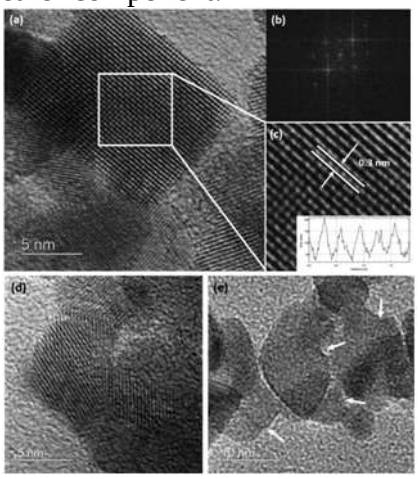

Fig. 6. (a) HRTEM image of a SnO_2 sample prepared at 180 °C along with (b) its Fourier transform; (c) detail of the image showing lattice fringes with spacing ~0.3 nm corresponding to the c axis dimension of rutile structured SnO2. Inset: Atomic density plot profile highlighting the spacing between lattice fringes; (d,e) HRTEM images showing the presence of screw and edge dislocations within NPs from this sample.

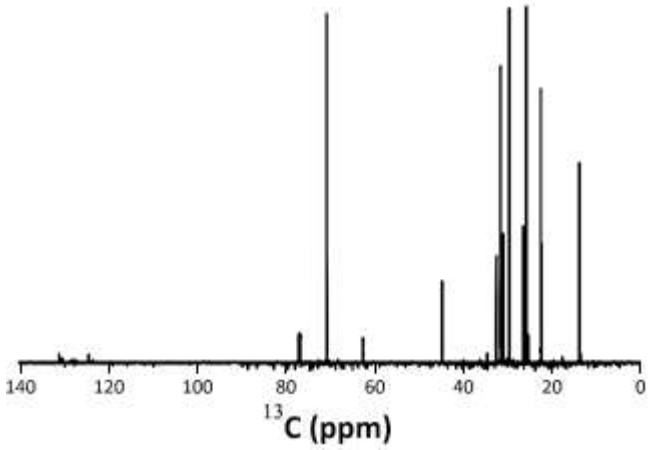

Fig. 7: ^{13}C NMR Spectrum of the reaction solution after Removal of the NPs.

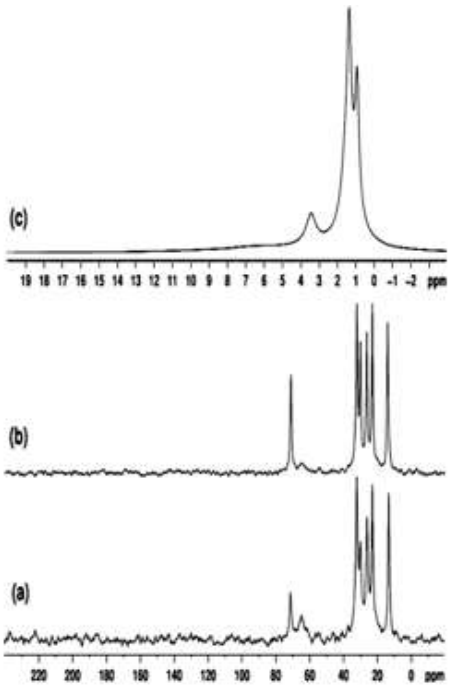

Fig.8. Proton-decoupled ^{13}C MAS (8 kHz) SSNMR spectra of samples prepared at (a) 160 and (b) 200 °C; (c) ^{1}H MAS (12 kHz) NMR spectrum of the sample prepared at 200 °C.

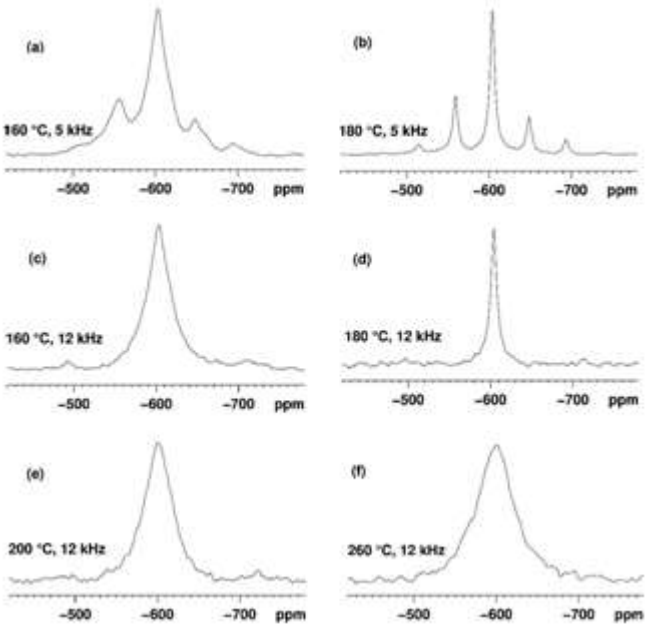

Fig. 9. ^{119}Sn MAS SSNMR spectra of SnO_2 samples prepared at (a) 160 °C (MAS 5 kHz); (b) 180 °C (MAS 5 kHz); (c) 160 °C (MAS 12 kHz); (d) 180 °C (MAS 12 kHz); (e) 200 °C (MAS 12 72Hhrs)

Our samples' ^{13}C MAS NMR spectra agree with the formation of 1-hexanol ($C_6H_{13}OH$) and dihexyl ether ($C_6H_{13}O\ C_6H_{13}$) species during the SnO_2 NP synthesis reaction, and indicate that these species stay bound to the solid SnO_2 NP samples even at the highest temperatures tested. A large signal at 64.9 ppm, which can be attributed to the C1 atom of 1-hexanol, can be seen in the spectra of the sample produced at 160 °C (Figure 8a). This occurs at a chemical shift of 63 ppm, which is higher than expected due to strong H-bonded interactions between the SnO_2 NP surface and the atoms of the molecule. There are six inequivalent carbon habitats (C_1C_6) of the hexyl (C_6H_{13}) fragments, which account for

the narrow signals found at 72.5, 32.3, 30.1, 26.2, 23.1, and 13.3 ppm, and 71.4, 32.5, 30.4, 26.6, 23.3, and 14.3 ppm for the 200 °C sample (Figure 8b). The observed change at 72 ppm from CH2OH to $CH_2OCH_2C_5H_{11}$ environments is suggestive of dihexyl ether production. In keeping with this assignment, the chemical shift of the C1 carbon should be influenced by an extra -effect of roughly +10 ppm from the $CH_2C_5H_{11}$ substituent (by analogy with the -effect of the methyl group). Samples generated at 160 and 200 °C show ^{13}C shifts of 71.05, 31.85, 29.90, 26.01, 22.71, and 14.02 ppm which are consistent with previous reports for dihexyl ether in $CDCl_3$ solution. Previous studies with 13C NMR have established the prevalence of such large frequency changes.

Table 3. Optical Band Gap (E_g) of the SnO_2 NP Specimens, as Calculated from the UV−Vis Data Using the Tauc Procedure

	optical E_g (eV)	
synthesis temperature (°C)	direct, $\gamma = 1/2$	indirect, $\gamma = 2$
160	3.12 ± 0.02	2.22 ± 0.02
180	3.67 ± 0.03	2.90 ± 0.03
220	3.86 ± 0.03	3.30 ± 0.02
240	3.90 ± 0.02	3.40 ± 0.02
260	3.99 ± 0.02	3.53 ± 0.02

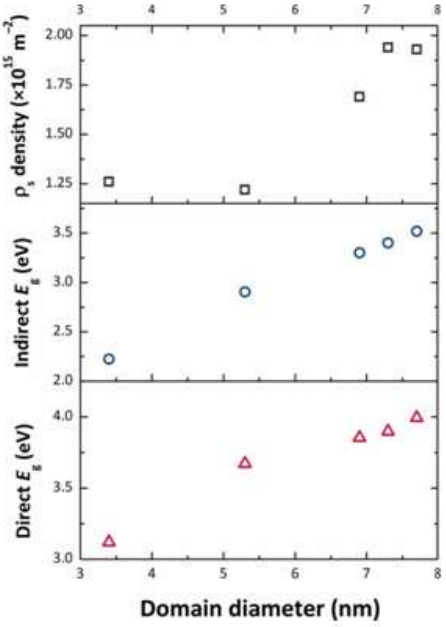

Fig. 10: Evolution of the optical gap E_g (bottom panel: direct E_g vs domain diameter; middle panel: indirect E_g vs domain diameter) and the screw dislocation density with the average domain diameter (top panel).

CONCLUSION

We have shown that crystalline SnO2 NPs may be synthesised in a single pot using a non hydrolytic sol-gel synthesis technique at temperatures as low as 160–260 °C. A potentially scalable technique is provided by using a commercially available short chain alcohol (1-hexanol) as the reaction medium and as one of the reagents, which results in SnO_2 NPs with very small and controllable NP sizes within a tight dispersion range. To produce SnO_2 NPs with controllable optoelectronic properties, a reaction between $SnCl_4$ and 1-hexanol is a green, cheap, and size-selected alternative to using hazardous and expensive precursors. We were able to build functionally active NPs, determine the NP sizes, and precisely detect screw dislocations within the SnO_2 NPs using the nonaqueous sol-gel process, WPPM

analysis of XRPD data, and HRTEM imaging. HRTEM imaging has further verified this to be the case.

By analysing UVvisible spectroscopy data, we were able to investigate shifts in the optical band gap Eg. In contrast to what was previously thought, our results showed that as NPs grew in size, Eg actually decreased relative to bulk SnO_2. Values estimated for particles >3.5 nm in size exceeded those of the bulk solid when a direct gap model for interband transitions was assumed, whereas values approaching those of the bulk were shown by indirect gap analysis for bigger NPs generated at higher temperatures. We propose that when NPs become larger, internal strain parameters are developed, which in turn cause an increase in screw dislocation densities observed at higher temperatures, accounting for the unanticipated fluctuation in Eg with an NP's size. Organic ligands bound to the surfaces of the expanding NPs during the synthesis step may be responsible for the internal stresses. The Eg of SnO_2 nanoparticles can be modified as a function of NP size, surface ornamentation, and the presence or relaxation of internal mechanical stresses, all of which can be controlled by our simple, low-cost synthetic technique. This strategy has the potential to improve the electrical characteristics and transparency to visible light of SnO_2 NPs for use in optoelectronic devices.

REFERENCES

1. Liu, X. et al. Tin oxide nanowires: synthesis, characterization, and gas sensing properties. J. Phys. Chem. B 108, 8266–8270 (2004).
2. Wang, W. et al. Tin dioxide nanowires as chemical sensors. Nature 419, 912–915 (2002).
3. Zhou, W. et al. Synthesis and gas-sensing properties of SnO_2 nanorods. J. Phys. Chem. C 112, 11169–11173 (2008).
4. Wu, W. et al. Electrospun SnO_2 nanofibers for high-performance gas sensor. J. Phys. Chem. C 113, 2229–2234 (2009).
5. Liu, X. et al. Tin oxide nanowires: synthesis, characterization, and gas sensing properties. J. Phys. Chem. B 108, 8266–8270 (2004).
6. Wang, W. et al. Tin dioxide nanowires as chemical sensors. Nature 419, 912–915 (2002).
7. Zhou, W. et al. Synthesis and gas-sensing properties of SnO_2 nanorods. J. Phys. Chem. C 112, 11169–11173 (2008).
8. Wu, W. et al. Electrospun SnO2 nanofibers for high-performance gas sensor. J. Phys. Chem. C 113, 2229–2234 (2009).Kulkarni, A., & Kulkarni, S. (2014). One-step synthesis of SnO_2 nanoparticles using a low-temperature nonaqueous sol-gel technique. Materials Science in Semiconductor Processing, 26, 291-297.
9. Srinivasan, S., & Kannan, R. (2016). Synthesis and characterization of SnO_2 nanoparticles by nonaqueous sol-gel method. Journal of Materials Science: Materials in Electronics, 27(6), 5606-5612.
10. Ravichandran, K., & Prakash, P. (2018). Low-temperature sol-gel synthesis of SnO_2 nanoparticles and their optical properties. Journal of Sol-Gel Science and Technology, 88(2), 255-265.
11. Sivakumar, S., & Ramasamy, P. (2019). One-step synthesis of SnO_2 nanoparticles using nonaqueous sol-gel method: Structural, optical and electrical properties. Materials Research Express, 6(6), 065017.
12. Rathod, D. S., & Jadhav, K. M. (2020). Synthesis and characterization of SnO_2 nanoparticles using a nonaqueous sol-gel technique. Journal of Nanoparticle Research, 22(4), 1-11.

13. Chakraborty, S., Chakrabarty, D., & Dutta, D. (2021). Low temperature synthesis of SnO_2 nanoparticles by nonaqueous sol-gel route and their photocatalytic activity. Journal of Environmental Chemical Engineering, 9(4), 105228.